Atomistic model of micelle-templated mesoporous silicas: structural, morphological and adsorption properties

(Article begins on next page)

24 April 2024

iris - AperTO

Atomistic model of micelle-templated mesoporous silicas: structural, morphological and adsorption properties

Benoit Coasne*,[†] and Piero Ugliengo[§]

[†] *Institut Charles Gerhardt Montpellier, UMR 5253 CNRS/UM2/ENSCM/UM1, 8 rue de l'Ecole Normale, 34296 Montpellier Cedex 05, France.* [§] *Dipartimento di Chimica, University of Torino, Via P. Giuria, 7. Torino, I-10125, Italy.*

*To whom correspondence should be addressed. E-mail: benoit.coasne@enscm.fr. Phone: +33 4 67 16 34 59.

Abstract. The structural, morphological and adsorption properties of MCM-41 porous silicas are investigated using a realistic numerical model obtained by means of *ab initio* calculations [P. Ugliengo et al., *Adv. Mater.* **2008**, *20*, 1]. Simulated X-ray diffraction, small angle neutron scattering, and electronic microscopy for the atomistic model are in good agreement with experimental data. The morphological features are also assessed from chord length distributions and porous volume and specific geometrical surface calculations, etc. The N_2, CO_2, and H_2O adsorption isotherms in the atomistic model of MCM-41 are also in reasonable agreement with their experimental counterpart. An important finding of the present work is that water forms a film adsorbed on specific hydrophilic regions of the surface while the rest of the surface is depleted in water molecules. This result suggests that the surface of MCM-41 materials is heterogeneous as it is made up of both hydrophilic and hydrophobic patches. While adsorption and irreversible capillary condensation can be described using the thermodynamical approach by Derjaguin (also known as the Derjaguin-Broekhoff-De Boer model), the Freundlich equation fits nicely the data for reversible and continuous filling in small pores.

1. Introduction

Siliceous porous materials such as MCM-41[1,2] still attract a great deal of attention because of their possible use as adsorbents or catalytic supports for gas adsorption, phase separation, catalysis, drug delivery, etc.[3,4,5] These materials are obtained by a template mechanism involving the formation of surfactant micelles in a mixture composed of a solvent and a silica source. After polymerization of the silica and removal of the organic micelles, one obtains a material made up of a hexagonal array of cylindrical pores. The pore size distribution is narrow with an average value that can be varied from 1.5 up to ~10 nm, depending on the synthesis conditions.[5] Properties of MCM-41 materials have been extensively studied by combining Transmission Electronic Microscopy (TEM), X-ray diffraction and adsorption experiments.[3,4] However, some uncertainties remain regarding the surface chemistry (presence of impurities, defects, etc.) as well as the surface texture (microporosity, surface roughness) of these materials.[6,7,8]

From a theoretical point of view, several attempts have been made to develop atomistic models of MCM-41 pores. Following the method proposed by Brodka and Zerda[9] and Pellenq and Levitz,[10] several authors obtained pores by carving cavities out of a block of amorphous or crystalline silica.[11,12,13] In order to mimic the silica surface in a realistic way, oxygen atoms at the pore surface are then saturated with hydrogen atoms. The materials obtained using such procedures can then be relaxed using simulated techniques such as simulated annealing in which the silica porous material is relaxed at high temperature and then slowly brought to ambient temperature.[14,15] Another possible approach to modeling porous solids is to mimic the synthesis process of the real material, a strategy used in the past[16] to develop realistic models for Vycor and controlled pore glasses. In particular, a top-down approach has been reported in the literature; one starts with on-lattice mesoscopic simulations of surfactant – solvent – silica

systems which allow reproducing the formation of hexagonal structure, resembling the arrangement of silica MCM-41 pores.[17] Then, the porous network obtained from such mesoscale simulations is carved out of atomistic silica in order to obtain fully atomistic models of the porous material that retains the morphology of the initial model. Such a procedure has been successfully applied in the past to model gas adsorption in realistic models of MCM-41 and SBA-15 materials.[18,19] Independently of the choice made among the approaches above, the question of how realistic the description of the surface chemistry in these classical models is remains to be answered. Of particular importance for modeling of adsorption in porous silica, the description of the surface chemistry in these models in terms of local geometry and ordering of the silica tetrahedra and surface termination (silanol groups, siloxane bridges, etc.) is crucial and has not been fully addressed in the literature.

Recently, one of us (P. U.) developed a realistic model of MCM-41 pores by using the density functional approach based on the rather accurate hybrid B3LYP functional.[20] This approach ensures an accurate enough description of the atomistic details of the inner surface of this material, particular as far as H-bonds between the surface Si-OH groups is concerned. The resulting model constitutes an important step in the modeling of adsorption in MCM-41 materials as it consists of a numerical model with surface chemistry (defects, surface termination, etc.) obtained using a method that allows taking into account the Quantum nature of chemical bonding. In contrast, other models of MCM-41 reported in the literature (which describe MCM-41 with more or less realistic features) rely on the use of classical forcefields which provide an approximated description of the chemical bonds treated using ab initio methods.

The aim of the present paper is to use this realistic model of MCM-41 pores in order to study the relationships between their structural, morphological, and adsorption properties. To do that, we first charaterize the structural properties of the realistic model of MCM-41 pores by simulating X-ray diffraction, small angle neutron scattering, and transmission electron microscopy. We also determine some morphological/textural properties by calculating chord length distributions, surface smoothness/roughness, porous volume, geometrical surface, etc. Then, using Grand Canonical Monte Carlo simulations, we study gas adsorption within the realistic model of MCM-41 pores and link its adsorption properties to its structural/textural properties. Three different gases N_2, CO_2, H_2O were selected as they involve different types of interaction with the silica surface (quadrupolar and dipolar interactions). In addition, these gases are relevant to different applications such as characterization of porous solids by means of nitrogen adsorption at low temperature, CO_2 capture, nanofiltration, etc.

2. Computational details

2.1. Model of Micelle-Templated Mesoporous Silicas

The model of micelle-templated mesoporous silica (MCM-41) was prepared according to the following procedure (full details can be found in Ref. 20). Starting from a hexagonal supercell of α-quartz containing about 600 atoms ($a = b = 4.06$ nm and $c = 1.22$ nm), a high-temperature classical molecular dynamics was conducted to force amorphization of the structure, carefully avoiding bond rupture and the formation of strained silica rings. In a second step, using the molecular graphics program MOLDRAW,[21] a hole of approximate hexagonal symmetry was created within the MCM-41 unit cell, and the unfilled valences of the inner hole walls were saturated with OH groups, resulting in a unit cell with 579 atoms ($Si_{142}O_{335}H_{102}$) and a tetrahedral-site (T-site) density of 8.2 T-sites/nm^3. As a final step, the internal coordinates of the starting structure were fully optimized at the B3LYP/6-31G(d,p)

5

level. **Figure 1**a shows the unit cell of the atomistic model of micelle-templated mesoporous silica MCM-41. Figure 1b shows a simulation box obtained by duplicating 5 times the unit cell corresponding to the black hexagon in the *x* and *y* directions. Further analysis of the structure reveals that the MCM-41 model has a surface density of silanol groups of 7.2 OH nm^2. Such a value is typical of models obtained by carving pores out of atomistic silica blocks. [10,12,22] It is important to note that, while significant relaxation occurs upon optimization, the pore remains overall an hexagonal shape. However, since the hexagonal shape of the pore was used as a starting point, it cannot be asserted that it corresponds to the most stable pore morphology in real MCM-41 samples.

2.2. Grand Canonical Monte Carlo simulations

We performed GCMC simulations to study adsorption of nitrogen at 77 K, water at 300 K, and CO2 at 303.15 K in the atomistic model of MCM-41 pores. The GCMC technique is a stochastic method that simulates a system having a constant volume *V* (the pore with the adsorbed phase), in equilibrium with an infinite reservoir of molecules imposing its chemical potential μ and its temperature *T*. The absolute adsorption/desorption isotherm is given by the ensemble average of the number of adsorbate molecules as a function of the fugacity *f* of the reservoir (the latter is determined from the chemical potential μ and temperature *T*). Nitrogen was described using the model of Potoff and Siepmann.[23] In this model, each nitrogen atom of the rigid nitrogen molecule is a center of repulsion/dispersion interactions which interact through a Lennard – Jones potential with the following parameter: $\sigma = 3.31$ Å and $\varepsilon = 36$ K. In addition, each nitrogen atom possesses a partial charge with $q = -0.482e$ that interacts through Coulombic forces. At the center of the nitrogen – nitrogen bond (the N – N interatomic distance is 1.1 Å), a partial charge $q = +0.964e$ compensates the negative charge on the

nitrogen atoms. Such a charge distribution reproduces the measured quadrupole moment of the nitrogen molecule. The Single Point Charge (SPC) model by Berendsen *et al.* was used for water in this work as it reasonably reproduces the structure and thermodynamics of bulk liquid water at ambient temperature.[24] In this model, water is represented as a rigid molecule: the hydrogen atoms are at a distance of 0.1 *nm* from the oxygen atom and the HOH angle is 109.47°. The oxygen atom is the center of a Lennard-Jones interaction potential. In addition, the atoms in the water molecule carry the following partial charges: -0.82e for the oxygen and +0.41e for each of the hydrogen atoms. The rigid model by Harris and Yung was used in this work to describe the carbon dioxide molecule.[25] The carbon – oxygen distance is 0.1149 *nm*. Each of the three atoms is a Lennard-Jones site which also carries a partial charge. All the interactions between the atoms of the adsorbate molecules (N_2, H_2O, CO_2) and the Si, O, H atoms were calculated by considering the intermolecular energy as the sum of the Coulombic and dispersion interactions with a repulsive short-range contribution. Full details on the interaction potential can be found in the supporting information file.

3. Results and Discussion

3.1. Structural Characterization

3.1.1. X-Ray Diffraction and Small Angle Neutron Scattering

Figure 2 shows the X-ray powder diffraction pattern for the realistic model of micelle templated mesoporous silica MCM-41. The latter diffraction pattern was calculated using Fullprof[26] applied to the configuration file with the positions of the Si, O and H atoms of the MCM-41 unit cell. The atomistic model of MCM-41 pores shows a diffraction pattern that is similar to the one recorded experimentally[1] with a first strong Bragg peak at 35 Å due to {100} plane reflections and three other strong Bragg peaks between 4 and 5 Å due to {110},

{200}, and {210} diffraction planes. It must be emphasized that the coincidence of the peak positions between the model and those for real samples results from the P6mm symmetry and from the size of the unit cell which were both imposed in our model.

Following previous works on numerical models of mesoporous silica,[10,18,19] small angle neutron scattering spectrum (SANS) was calculated for the realistic model of micelle-templated MCM-41. While X-ray diffraction patterns provide information about the spatial arrangement of the pores in the porous network, SANS allows assessing the textural properties of the surface of porous materials. In particular, the diffused intensity $I(Q)$ obtained at small Q values by means of SANS provides crucial information regarding the surface properties of the material in the Porod range, *i.e.*, $QD > 1$ (*D* is the pore width).[27] $I(Q)$ in a SANS spectrum can be calculated directly over the configuration of the *N* atoms of the MCM-41 model:

$$I(Q) = \frac{1}{2\pi N} \left| \sum_{i=1}^{N} b_i \exp\left(i\vec{Q}.\vec{r_i}\right) \right|^2 \qquad (1)$$

where $\vec{r_i}$ is the position of atom *i* and b_i its neutron coherence length ($b = 4.1491\times10^{-15}$ *m*, 5.803×10^{-15} *m*, -3.739×10^{-15} *m* for Si, O, and H atoms, respectively). The SANS spectrum for the model of micelle-templated mesoporous silica is shown in **Figure 3**. Peaks obtained at large momentum transfer ($Q > 1$ Å^{-1}) are in very good agreement with those obtained for bulk amorphous silica ~ 1.5 Å^{-1}, 3.0 Å^{-1}, 5.25 Å^{-1} and 8.0 Å^{-1}.[28] The SANS spectrum in Figure 3 was fitted using an algebraic decay law $I(Q) \sim Q^{-x}$ over the range 0.1-0.8 Å^{-1} in order to determine the Porod exponent that characterizes the surface roughness of the porous solid at length scales ~8 – 62 Å. *x* was found equal to 3.2 +/- 0.2. This Porod exponent, which is lower than the value $x = 4$ for cylindrical pores having a smooth pore/void interface with

atomistic surface roughness only, is typical of disordered porous silicas such as Vycor[29,30] or silica gels.[6,31] Such a value is also in agreement with SAXS or SANS experiments for MCM-41 materials.[6,8] Edler et al.[8] reported that the Porod exponent for MCM-41 samples is in the range 3.0-3.5. This result was confirmed later by Sonwane et al.,[6] who showed that the Porod exponent for MCM-41 samples of different pore sizes is in the range 3.4-3.6 at length scales 20-50 Å.

3.1.2. Transmission Electron Microscopy

In the spirit of the work by Pikunic et al. on atomistic models of activated porous carbons,[32] we simulated transmission electronic microscopy (TEM) of the realistic model of micelle-templated mesoporous silica MCM-41. In this model, the material is assumed to be quasi-amorphous as it allows neglecting diffraction contrast due to crystalline registry. Given the amorphous nature of the mesoporous silicas considered in the present work, the latter assumption is reasonable. We chose to align the electron beam with the z direction of the simulation box which corresponds to the pore axis in the model of MCM-41 mesoporous silica. The TEM image, which is perpendicular to the electron beam, is divided into a two-dimension grid where each grid point is a bin (the bin size is 0.2 *nm* × 0.2. *nm*). Then, we project the center of each atom of the mesoporous silica material onto the 2D grid and add one to each point of the histogram that is within a circle equal to the van der Waals diameter of the atom (σ = 3.804 Å, 3.033 Å, and 2.846 Å for the Si, O, and H atoms, respectively). In order to simulate the thermal atomic motion, we slightly and randomly moved each atom of the silica material (the maximum displacement is ±0.5 Å in each direction x, y, and z). The relative intensity $\Delta I/I$ of each histogram point is calculated by applying the Beer-Lambert law to each histogram bin:

$$\frac{\Delta I}{I} = 1 - \sum_i \exp(-\alpha_i N_i) + \xi \qquad\qquad (2)$$

where N_i is the total number of atoms of type i = Si, O, or H projected to the histogram bin and α_i a constant proportional to the elastic scattering cross section of species i. In this work, the simulated images, which are nearly insensitive to the values α_i, were obtained for α_i equal to the atomic number of the element i (Z_i). ξ in Eq. (2) consists of a random number in the range [0,0.333] which we added to the relative intensity $\Delta I/I$ in order to simulate the electronic noise generated by the TEM apparatus. While the use of such a contribution is not crucial, it allows reproducing the noise observed on any real TEM image (*i.e.*, void regions in real images of porous materials always appear with a non zero contrast). **Figure 4** shows the simulated TEM image obtained using the procedure above for the atomistic structural model of micelle-templated mesoporous silica MCM-41. The latter was obtained by plotting in grey scale the contour map corresponding to the relative intensity $\Delta I/I$ of each histogram point. We also show in **Figure 4** the experimental TEM image of MCM-41 materials having a pore diameter D = 2.0 nm.[33] In both images, the darker areas represent the pore walls while lighter areas represent the pore voids and areas with low densities. The TEM image for the atomistic model of the micelle-templated mesoporous silica captures all the features of the TEM image for the real sample. One clearly sees the hexagonal arrangement of cylindrical pores having a uniform pore size. In addition, granular textures at the pore surface are observed in both the simulated and experimental images. The latter are often interpreted as experimental evidence of atomistic surface roughness or the presence of micropores in the pore walls. While the simulated image in **Figure 4** was obtained for a numerical material having no micropores, granular features similar to those in experimental TEM images are observed. The latter result suggests that the observation of granular textures does not necessarily coincide with the

presence of micropores within the pore walls. The pore wall density and thickness of the atomistic model of MCM-41 materials will be discussed in more details later in this paper.

3.2. Morphological Characterization

3.2.1. Chord Length Distributions

Chord length distribution analysis is a useful tool to characterize porous materials as it allows estimating the pore size distribution, pore wall thickness distribution, specific surface area, etc.[10,34] A chord length distribution can be obtained using the following procedure. A great number of lines with random directions and origins and different lengths are thrown through the porous material. The histogram $P(l_m)$ of the chord lengths in the matrix l_m and the histogram $P(l_p)$ of the chord lengths in the pore voids l_p are then accumulated. These two chord length distributions correspond to the pore wall thickness and pore size distributions, respectively. In what follows, in order to locate the interface between pore voids and pore walls, we assumed that a point belongs to the pore matrix if it is located at a distance less than $\delta = 3.6$ Å from any of the matrix atom (such a value roughly corresponds to the size of the N_2 molecule). Respectively, a point belongs to the pore voids if it is located at a distance greater than $\delta = 3.6$ Å from all of the matrix atoms. The specific surface area S_{sp} of the porous material can be obtained from: [10]

$$S_{sp} = \frac{4\phi}{\langle l_p \rangle \rho} \tag{3}$$

where $\langle l_p \rangle = \int_0^\infty l P(l) dl$ is the average value of the in-pore chord length distribution while $\rho = 1.35 \ g/cm^3$ and $\phi = 0.623$ are the matrix density and porosity of the atomistic model of MCM-41 materials, respectively. Figure 5 shows the in-pore and in-wall chord length distributions for the atomistic model of micelle-templated mesoporous material MCM-41. The

average in-pore and in-wall chord lengths are $\langle l_p \rangle = 17.8$ Å and $\langle l_m \rangle = 22.6$ Å, respectively.

The in-pore chord distribution exhibits a maximum value at $l_p^{\max} = 26$ Å which is close to the size of the pores in the atomistic model of MCM-41 materials. In fact, the latter value is an estimate of the pore size diminished by two times the criterion used to locate the interface. If we define the pore size D_p as the distance between the center of mass of H atoms at the pore surface, one gets $D_p = l_p^{\max} + 2\delta = 33.2$ Å. The in-wall chord length distribution exhibits a maximum value at $l_m^{\max} = 16.5$ Å which provides an estimate of the pore wall thickness. Again, if we define the pore wall thickness from the distance between the center of mass of the H atoms of the matrix (*i.e.*, without taking into account the van der Waals diameter of the matrix atoms), one gets $D_m = l_m^{\max} - 2\delta$ Å = 9.3 Å (for $\delta = 3.6$ Å). A second peak is observed at $l \sim 45 - 50$ Å in the in-wall chord length distribution. The latter corresponds to the wall thickness in the direction perpendicular to the pore surface (*i.e.*, the length of the segments constituting the porous material when viewed along the *z*-axis). Comparison between these estimates and the pore size and pore wall thickness obtained from other geometrical techniques and adsorption-based techniques will be provided below. Using equation (3), we found that the specific surface of the atomistic model of MCM-41 materials is $S_{sp} = 1034$ m^2/g.

3.2.2. Geometrical Specific Surface and Porous Volume

As discussed in the previous section, locating the interface between pore voids and pore walls requires using a criterion which is somewhat arbitrary. In order to determine the influence of the choice for this interface criterion δ, we estimated the pore volume V_{sp} and specific surface S_{sp} as a function of δ (*i.e.*, accessible to an adsorbate molecule whose distance to any matrix atom cannot be smaller than δ). The specific surface $S_{sp}(\delta)$ was estimated as the surface

covered by the *center of mass* of an adsorbate molecule of a size δ as it rolls over the pore

surface (see the blue line in Figure 6). Such a surface departs from Connolly's surface[35] which

corresponds to *the contact surface* covered by the adsorbate molecule as it rolls over the pore

surface (see the red line in Figure 6). In this work, instead of estimating Connolly's surface,

we estimated S_{sp} as it is consistent with the definition of the BET surface which is defined

from the number of molecules needed to form an adsorbed monolayer on the pore surface. S_{sp}

can be estimated using the following Monte Carlo procedure. Many random lines $l = \{l_1, l_2, l_3,$

$..., l_n)$ are thrown within the porous material enclosed in the simulation box. Each line l_i

intersects p_i times with the pore surface, $p = \{p_1, p_2, p_3, ..., p_n)$ (Figure 6). The specific

surface area per unit volume is given by:[19]

$$S_{sp}(\delta) = 2\frac{\sum\limits_{i=1}^{n} p_i}{\sum\limits_{i=1}^{n} l_i} \qquad (4)$$

The porous volume $V_{sp}(\delta)$ was estimated using a Monte Carlo scheme in which many points N

are randomly selected within the porous volume. Let N_p be the number of points falling within

the pore voids, *i.e.* points located at a distance greater than $\delta/2$ from all of the matrix atoms

(see Figure 6). The fraction N_p/N provides an estimate of the porosity $\phi(\delta)$ as seen by an

adsorbate molecule whose characteristic approach distance to the matrix atoms is δ. The

porous volume is then obtained by multiplying the porosity by the total volume of the porous

material V, $V_{sp}(\delta) = \phi(\delta)V$.

Figure 7 shows $V_{sp}(\delta)$ and $S_{sp}(\delta)$ as a function of δ for the atomistic model of MCM-41

materials. For small δ, $S_{sp}(\delta)$ increases with increasing δ as the surface of each matrix atom

increases as $4\pi r^2$. We note that the smallest adsorbate molecules have sizes which are already

large enough to not access the physical region between matrix atoms ($\delta \sim 0.29$ *nm* for helium and $\delta \sim 0.28$ *nm* for H_2). As $\delta > 0.15$ nm, $S_{sp}(\delta)$ decreases with increasing δ as the adsorbate molecule becomes too big and does not "see" the atomic surface roughness of a size smaller than δ. Interestingly, the value $S_{sp}(\delta) = 920$ m^2/g for $\delta = 3.6$ Å is close to that obtained using Eq. (3) in which the average in-pore chord length distribution is that calculated using the same δ value (1034 m^2/g). In contrast to $S_{sp}(\delta)$, $V_{sp}(\delta)$ varies in a continuous manner with δ as the porous volume accessible to the adsorbate molecule nessarily decreases with increasing its minimum approach distance to the matrix atoms. The pore hydraulic diameter can be readily obtained from $S_{sp}(\delta)$ and $V_{sp}(\delta)$:

$$D_{hyd}(\delta) = 4\frac{V_{sp}(\delta)}{S_{sp}(\delta)} \tag{5}$$

For $\delta = 3.6$ Å, we found $D_{hyd} = 29$ Å which is close to the pore size $D_p \sim 25$ Å defined from the first moment of the in-pore chord length distribution.

3.2.3. Silica wall thickness and roughness

Determining the silica wall thickness and atomic surface roughness of real MCM-41 materials is a non-straightforward task. From an experimental point of view, the silica wall thickness d_w, which is usually determined from TEM images, is a crucial parameter as the pore size can be estimated from the distance d_{100} between (100) diffraction planes dimished by d_w. While the pore surface disorder at length scales $\sim 1 - 10$ *nm* can be estimated using the Porod exponent obtained from small angle scattering (see section 3.1.1), the atomic surface disorder (a few Å) cannot be assessed directly. In order to determine the average silica wall thickness and atomic surface roughness of the realistic model of MCM-41 materials, we show in Figure 8 a density contour plot of the silica wall. The color scale varies linearly with the density in

g/cm^3. This density contour plot was estimated by calculating the density on a 2D grid in the (x,y) plane. On each grid site, the density was calculated in a volume $\Delta V = \Delta x \Delta y L_z$ where $\Delta x = \Delta y = 0.4$ *nm* while $L_z \sim 3.6$ *nm* is the box size along the *z*-direction. The latter volume was chosen as an optimal value between accuracy and statistics: small volumes are needed to estimate subtle density fluctuations but require accumulating significant statistics while large volumes do not require accumulating significant statistics but cannot be used to estimate subtle density fluctuations. As expected for amorphous silica materials, the density in the middle of the pore wall is about $\rho = 2.2$ g/cm^3. In contrast, the density at the pore surface can be as low as $\rho = 0.5$ g/cm^3 due to important surface roughness (which is sometimes described as intrawall microporosity). To further characterize the silica wall thickness and density variations, we show in Figure 8 the density histogram $P(\rho)$ defined as the percentage of wall domains of a density comprised between $\rho - \Delta\rho$ and $\rho + \Delta\rho$ with $\Delta\rho = 0.1$ g/cm^3. The density histogram shows that the silica walls in the atomistic model of MCM-41 materials can be decomposed into two domains. (1) The heart of the silica walls is composed of bulk-like amorphous silica with a density varying between 1.6 and 3.6 g/cm^3 and an average density of 2.25 g/cm^3. (2) The domain corresponding to the pore surface, which is less dense than the heart of the silica walls, has a density varying between 0.2 and 1.6 g/cm^3 with an average density of 0.67 g/cm^3. Defining the pore wall thickness as the size of domains where the density is larger than 1.0 g/cm^3, we found d_w varying between 8 and 9.4 Å. The latter values are consistent with the pore wall thickness estimated from the average in-wall chord length distribution $D_m = 9.3$ Å (see section 3.2.1).

3.3. N_2, CO_2, and H_2O adsorption

In this section, we study gas adsorption within the realistic model of MCM-41 pores and link its adsorption properties to its structural/textural properties. Three different gases N_2, CO_2,

H_2O were selected as they involve different interaction types with the silica surface (quadrupolar and dipolar interactions). For each gas, we also propose a simple model which allows describing the adsorption isotherm. We also discuss the validity of simple characterization techniques such as the BET model. Only adsorption data are shown/discussed in this paper as the nature of capillary evaporation observed in our simulations departs from what is expected in real experiments. Indeed, due to the use of periodic boundary conditions in our model of MCM-41 materials, the pores are equivalent to pores of an infinite pore length. Consequently, the confined fluid in our model cannot evaporate at equilibrium and the pore necessarily empties through cavitation *i.e.* the spontaneous nucleation of the gas phase within the pore. In contrast, for real MCM-41 materials, the confined liquid is physically connected to the external phase through pore openings so that desorption occurs at equilibrium by the displacement of a gas/liquid meniscus along the pore axis (for a discussion on the effect of physical connections to the external phase, see Ref. 12). The MCM-41 model used in the present work could be modified to make it of a finite length and with an interface with the external phase but, to do that, one would have to make some assumptions to model its external surface (about the number, position and orientation of the OH groups for instance). As a result, we decided to keep the realistic model as reported in Ref. 20 and not to look at the desorption/evaporation process. Adsorption/condensation provide enough information on how realistic is the surface of the present model as far as nitrogen, water and carbon dioxide adsorption in MCM-41 pores are concerned.

3.3.1. Adsorption isotherms

Figure 9 shows the N_2 adsorption isotherm at 77 K in the atomistic model of micelle-templated mesoporous silica MCM-41. Such an adsorption isotherm conforms the classical picture of adsorption and capillary condensation in nanopores. At low pressures, a molecular

thick film is adsorbed at the pore surface. The thickness of the adsorbed film increases with increasing pressure in the multilayer adsorption regime. Then, at a pressure $P = 0.25 \, P_0$ much lower than the bulk saturating vapor pressure, a sharp increase in the adsorbed amount is observed as capillary condensation occurs within the nanopores. The insert in Figure 9 shows the isosteric heat of adsorption Q_{st} as a function of the adsorbed amount of N_2 in the atomistic model of MCM-41 pores. The latter curve is characteristic of adsorption of simple gases on heterogeneous surfaces; Qst ~ 14 kJ/mol at low loading (when strongly adsorbing sites are being filled) and then decreases in a continuous way to a value close to the heat of liquefaction of nitrogen (7 kJ/mol) as further adsorption takes place. As is usually expected, Q_{st} increases as condensation occurs due to the heat released as the gas/liquid interface within the pore disappears.

We also show in Figure 9 experimental data by Jaroniec and coworkers[33] for nitrogen adsorption at 77 K in MCM-41 materials having a pore size (D = 3.6 nm) similar to that of the atomistic model considered in the present work. Given that the numerical and experimental samples have different densities and porosities, the experimental data have been multiplied by a constant so that the experimental adsorbed amount when the pores are filled (*i.e.*, above capillary condensation) corresponds to the value observed for the atomistic model of MCM-41 materials. Prior to capillary condensation, the adsorbed amounts for the atomistic model are in good agreement with the experimental data. This result suggests that the surface of the atomistic model accurately describes the specific interaction between nitrogen and hydroxylated silica surfaces. The fact that the condensation pressure in the simulated data overestimates the experimental value can be explained as follows. The steepness of the experimental adsorption branch at the pressure where capillary condensation occurs indicates that the temperature T = 77 K is below the critical capillary temperature T_{cc} (*i.e.*, the

temperature above which capillary condensation is replaced by continuous and reversible pore filling). On the other hand, the reversibility of the experimental adsorption isotherm suggests that T is above T_{ch}, which is defined as the temperature above which fluctuations are large enough to avoid the system to be trapped in a metastable state upon adsorption. Therefore, for such temperatures $T_{ch} < T < T_{cc}$, the adsorption isotherm still exhibits capillary condensation but the latter occurs at the equilibrium transition pressure, *i.e.* the pressure at which capillary evaporation is observed. In contrast, capillary condensation in our simulations, in which fluctuations are smaller than in the experiments due to finite sampling of the phase space, occurs close to or at the spinodal limit of the adsorption process and is therefore located at a pressure larger than the at equilibrium transition pressure. Moreover, we cannot rule out that the pore size in the experimental data can be slightly lower than the value of 3.6 nm (the latter, which relies on the use of a model to relate condensation/evaporation pressures and pore size, are given within an error bar).

Nitrogen adsorption at low temperature is a routine characterization technique of nanoporous materials.[36] For instance, the specific surface of porous materials is usually assessed from adsorption experiments (prior to capillary condensation of the fluid) on the basis of the Brunauer, Emmett and Teller (BET) method. Figure S1 in the supporting information shows the BET plot corresponding to the N_2 adsorption isotherm at 77 K in the atomistic model of MCM-41 materials. The BET model fits very well the simulated data with a correlation coefficient R2 = 0.999. We found $S_{BET} \sim 1000$ m^2/g (the latter value is obtained by multiplying N_0 by the surface area occupied by an adsorbed nitrogen molecule, $a_{N2} = 0.162$ nm^2) and $C = 100$. The value obtained for C is consistent with the values that are usually reported in the literature for oxide surfaces, $C \sim 80 - 150$. It is interesting to note that the BET surface, S_{BET}, is in reasonable agreement with that, $S_{sp} = 920$ m^2/g, determined from the chord

length distribution and/or accessible surface area using $\delta = 3.6$ Å (which roughly corresponds to the size of the nitrogen molecule). This result shows that, in agreement with our previous work on nitrogen in regular silica nanopores, the BET model provides reasonable estimates of the surface area of porous materials. The fact that the BET surface slightly overestimates the surface area obtained from mathematical procedures supports the suggestion made by some authors[37] to use a smaller value for a_{N2} (0.135 nm^2 instead of 0.162 nm^2). Nitrogen adsorption at low temperature is also routinely used to estimate the porous volume (and, hence, the porosity) of porous materials. Using the nitrogen bulk density, we estimated that the maximum amount of N_2 molecules adsorbed in the atomistic model of MCM-41 pores corresponds to a porous volume $V = 0.61$ cm^3/g. Again, such a value is in agreement with the specific porous volume determined using the Monte Carlo procedure described in section 3.2.2. when using $\delta = 3.6$ Å (~ the size of the nitrogen molecule). This result shows that determining the porous volume of nanoporous silicas by converting the maximum adsorbed amount using the bulk density is a reasonable approximation.

Figure 10 shows the water adsorption isotherm at room temperature in the atomistic model of MCM-41 materials. As in the case of nitrogen adsorption at 77 K, such an adsorption isotherm conforms the classical picture of adsorption in large nanopores. In contrast to the nitrogen adsorption isotherm discussed above, the water adsorbed amount increases very slowly with increasing pressure in the low pressure range. This result suggests that the surface of the atomistic model of MCM-41 pores is hydrophobic. Such a result is confirmed by the isosteric heat of adsorption curve (see insert in Figure 10) which shows that Q_{st} at low loading is less than the cohesive energy of bulk liquid water (~ 44 kJ/mol). In fact, we found that the surface of the atomistic model of MCM-41 pores is composed of both hydrophilic and hydrophobic patches. This can be clearly seen in Figure 11 where we report a typical

molecular configuration showing that water forms a film adsorbed on specific hydrophilic regions of the surface while the rest of the surface is depleted in water molecules. It seems that a few water molecules will first adsorb onto hydrophilic defects at the pore surface. In turn, such small clusters of adsorbed water molecules will constitute hydrophilic regions on which other molecules will get adsorbed upon increasing the pressure. Although such a result was obtained without allowing the OH surface groups to relax upon adsorption, we believe that it is relevant as we found in a recent work that relaxing the OH groups does not lead to a big difference in terms of water adsorption on flat silica surfaces.[15] Moreover, the fair agreement between our results and available experimental data (see below) suggests that water adsorption in MCM-41 is reasonably described using the present model. Note that such a dual hydrophilic/hydrophobic nature of surfaces has been recently observed in the case of talc surfaces[38] (see also Ref. 15 for a detailed discussion on the effect of surface hydroxylation on the hydrophobic/hydrophilic nature of silica). We also show in Figure 10 experimental data by Inagaki[39] for water adsorption at room temperature in MCM-41 materials. The pore size of the MCM-41 sample in Ref. 39 is not reported; however, given that the N_2 adsorption isotherm for the MCM-41 in Ref. 39 is very close to that of Jaroniec and coworkers in Figure 9, we assume that the two samples have similar pore sizes which are close to that of the atomistic model of MCM-41 pores considered in the present work. The simulated water adsorption isotherm is in very good agreement with the experimental data by Inagaki et al. (similar agreement was reached when considering the data by Chen et al.[40]). This result suggests that the atomistic model of MCM-41 pores capture both the formation of an adsorbed film and capillary condensation of water at room temperature in real MCM-41 samples. Assuming that the density of confined water equals the bulk density of liquid water (1 g/cm^3), we found that the porous volume of the atomistic model of MCM-41, determined from the maximum amount of adsorbed water molecules, is 0.59 g/cm^3. Such a value is very

close to that determined from nitrogen adsorption, which suggests that both low temperature nitrogen adsorption and room temperature water adsorption can be used to assess the porosity of nanoporous materials.

Figure 12 shows the CO_2 adsorption isotherm at room temperature in the atomistic model of MCM-41 materials. In contrast to what was observed for nitrogen and water, the CO_2 adsorption isotherm is reversible and continuous as capillary condensation in such nanopores is suppressed. The disappearance of capillary condensation can be explained as follows. For a given pore size, there is a temperature called the critical capillary temperature (T_{cc}) above which the adsorption isotherm becomes reversible and continuous.[41] T_{cc} increases as the pore width H increases following the formula $\dfrac{\Delta T_c}{T_c} = \dfrac{T_c - T_{cc}}{T_c} \approx \dfrac{2\sigma}{H}$ where T_c is the bulk critical temperature and σ the molecular size of the fluid molecule. The fact that the CO_2 adsorption isotherm in the model of MCM-41 pores is reversible and continuous shows that CO_2 is above its capillary critical temperature. The insert in Figure 12 shows the isosteric heat of adsorption Q_{st} as a function of the adsorbed amount of CO_2 in the atomistic model of MCM-41 pores. Again, the latter curve is characteristic of the adsorption of simple fluids on heterogeneous surfaces; Qst ~ 21 kJ/mol at low loading and then decreases in a continuous way to ~10 kJ/mol as the adsorbed amount increases up to 10 mmol/g. For large adsorbed amounts, Q_{st} increases as the fluid – fluid contribution to the total isosteric heat of adsorption increases with increasing the density of confined fluid. We also show in Figure 12 experimental data by Ho et al.[42] for CO_2 adsorption at room temperature in MCM-41 materials having a pore size $D = 3.5$ nm, which is close to that of the atomistic model of MCM-41 pores considered in the present work. The simulated CO_2 adsorption isotherm is in good agreement with the experimental data. This result is consistent with the previous work by Ho et al.[42] in which it

was found that molecular simulation of CO_2 adsorption in atomistic silica pores reproduces experimental data.

3.3.2. Theoretical models of adsorption in MCM-41

With the aim of providing a theoretical picture of adsorption and desorption in regular silica nanopores, we consider the thermodynamical approach by Derjaguin also known as the Derjaguin-Broekhoff-De Boer model.[43,44,45] The Grand Potential of the system composed of the pore of length L and radius R and the film of a thickness e adsorbed at the pore surface writes:

$$\Omega = -P_G V_G - P_S V_S - P_L V_L + \gamma_{SL} A_{SL} + \gamma_{LG} A_{LG} + A_{LG} W(e) \qquad (6)$$

where P_G, P_L, P_S, $V_G = \pi L(R - e)^2$, $V_L = \pi L(R^2 - (R - e)^2)$, V_S are the pressure and volume of the gas, adsorbed, and solid phases, respectively. γ_{LG}, γ_{SL} and $A_{LG} = 2\pi L(R - e)$, $A_{SL} = 2\pi LR$ are the gas-adsorbed phase and solid-adsorbed phase surface tensions and surface areas, respectively. The interface potential $W(e)$ in Eq. (6) allows describing adsorption at the surface of the material as it accounts for the interaction between the adsorbate molecule and solid surface. We note in passing that $W(e)$ is related to the disjoining or solvation pressure $\pi(e)$ which is often invoked to describe adsorption phenomena and deformation of porous materials:

$$\pi(e) = -\frac{dW(e)}{de} = P_G - P_L \qquad (7)$$

In the case of adsorption in cylindrical pores, Saugey and Charlaix have shown that $W(e)$ deriving from van der Waals forces can be expressed as:[46]

$$W(e) = \frac{A_{SLV}}{12\pi(R-r)^2} \frac{2r(R^2+r^2)}{R(R+r)^2} \qquad (8)$$

where $r = R - e$ and A_{SLV} is the Hamaker constant for the adsorbate – adsorbent being considered. After inserting Eqs. (7) and (8) in Eq. (6) and assuming $P_S V_S$ is constant (*i.e.*, the volume free energy of the solid is not modified upon adsorption), one can estimate the thickness of the adsorbed film e at a given bulk gas pressure by minimizing Ω with respect to e, *i.e.* $\frac{d\Omega(e)}{de} = 0$. The Grand free energy exhibits two minima at low gas pressures. The stable solution $e \neq 0$ consists of a configuration where a film of thickness e is adsorbed at the pore surface and in equilibrium with the gas phase located in the pore center. The metastable solution $e = R$ corresponds to the situation where the pore is completely filled with the liquid. As the pressure increases, the thickness of the adsorbed film increases and the minimum $e \neq 0$ is shifted toward the pore centre $e = R$. The equality of the two minima $\Omega(e \neq 0) = \Omega(e = R)$ defines the equilibrum transition pressure, P_e, where capillary evaporation occurs. From a mathematical point of view, P_e must verify $\frac{d\Omega(e)}{de} = 0$ and $\Omega(e \neq 0) = \Omega(e = R)$. For pressures above P_e, $\Omega(e)$ still exhibits two minima but the deepest solution is located at $e = R$, which corresponds to the pore being completely filled with the liquid. The minimum $e \neq 0$ (adsorbed phase + gas) now corresponds to a metastable state. The pressure, P_c, at which the latter minimum disappears corresponds to the limit of metastability of this solution; spontaneous nucleation of the liquid phase occurs within the pore as the pressure reaches P_c. P_c is given by the following conditions $\frac{d\Omega(R)}{dR} = \frac{d^2\Omega(R)}{dR^2} = 0$. It is worth noting that the model above is an alternative approach to the modified Kelvin equation used in standard pore characterization methods, which include *ad hoc* corrections for the presence of an adsorbed film. In contrast, the general approach above includes *de facto* the adsorbed film and allows

predicting the dependence on the gas pressure of its thickness e. We also note that one recovers the Kelvin equation by omitting $W(e)$ in the general approach above. Finally, we note that Pellenq and coworkers recently developed a similar model which allows taking into account the effect of temperature on the width of capillary condensation hysteresis.[47]

The general model above can be used to calculate entire adsorption/desorption isotherm including condensation and evaporation phenomena. On the other hand, as will be discussed below, this model cannot be applied when adsorption/desorption is reversible and continuous (*i.e.*, when capillary condensation is suppressed because of drastic confinement such as in very small nanopores). Figure 9 shows the predictions of the Derjaguin-Broekhoff-De Boer model approach for nitrogen adsorption at 77 K in a cylindrical nanopore having the same diameter than the atomistic model of MCM-41 materials. The parameter $A_{SLV} = -10^{-19}$ J/m^2 was adjusted to reproduce the simulated adsorption isotherm at low pressures (A_{SLV} is the only adjustable parameter of the model). The model is in fair agreement with the simulated adsorption isotherm prior to capillary condensation. In particular, the model reproduces the relative height of the hysteresis defined as the ratio of adsorbed amount prior to capillary condensation (or evaporation) to the adsorbed amount when the pore is filled. The fact that the capillary condensation pressure predicted in the model overestimates that observed in the simulation can be explained as follows. In both sets of data, condensation is a metastable transition which occurs as fluctuations become large enough to make the cylindrical film adsorbed at the pore surface collapse. While condensation is assumed to occur at the end of the metastability region (spinodal curve) in the theoretical approach, condensation in the simulations can occur prior to the end of this region due to larger fluctuations. As far as capillary evaporation is concerned, the simulated and theoretical data cannot be compared; pore emptying occurs at equilibrium in the theoretical approach (displacement of a gas/liquid

meniscus along the pore axis) while it occurs through cavitation (metastable transition) in the simulations. In fact, equilibrium desorption in the simulation data is necessarily located between the metastable condensation and cavitation pressures, which is captured by the Derjaguin-Broekhoff-De Boer thermodynamical model. Figure 10 shows the predictions of the Derjaguin-Broekhoff-De Boer model for water adsorption at 300 K in a cylindrical nanopore having the same diameter than the atomistic model of MCM-41 materials. Again, the parameter $A_{SLV} = -5 \times 10^{-22}$ J/m^2 was adjusted to reproduce the simulated adsorption isotherm at low pressures. As was observed for nitrogen adsorption, the model is in fair agreement with the simulated data and reproduces both the adsorbed amounts prior to capillary condensation and the capillary condensation pressure. As discussed above, the fact that the condensation pressure in the simulated data or in the proposed model overestimates the experimental value for nitrogen at 77 K can be explained as follows. The shape of the experimental adsorption isotherm (*i.e.*, reversible capillary condensation) suggests that the temperature T is such that $T_{ch} < T < T_{cc}$. As a result the adsorption isotherm still exhibits capillary condensation but the latter occurs at the equilibrium transition pressure, *i.e.* the pressure at which capillary evaporation is observed. In contrast, capillary condensation in our simulations or in the proposed model occurs close to or at the spinodal limit of the adsorption process and is therefore located at a pressure larger than the at equilibrium transition pressure. The fact that both our simulations and theoretical model describe well the water adsorption isotherm suggests that the temperature is well below T_{ch} so that capillary condensation in the experiments occur close to the spinodal limit as predicted in our simulations or in the theoretical model.

We now discuss the theoretical modeling of the adsorption isotherm of CO_2 at room temperature in the atomistic model of MCM-41 pores. While the adsorption isotherms for

nitrogen and water in the atomistic model of MCM-41 materials could be modeled using the Derjaguin-Broekhoff-De Boer thermodynamic model, CO_2 adsorption at room temperature requires modeling using a different theoretical approach as capillary condensation is suppressed in this case (as discussed above, confined CO_2 in such small nanopores is above its capillary critical temperature[41]). The Freundlich adsorption isotherm is an empirical equation that relates the amount x of gas adsorbed on a surface to the gas pressure P: $x = KP^{1/n}$ where n and K are adjustable parameters. Figure 12 shows a fit of the simulated data for CO_2 adsorbed in the atomistic model of MCM-41 materials using the Freundlich equation. The latter is found to fit very nicely the simulated data for $n = 1.41$ and $K = 0.369$ $mmol/cm^3/Pa^n$. As is usually observed, the Freundlich equation overestimates the adsorbed amount at very high pressures due to the fact that it mathematically diverges for large pressures while the experimental adsorbed amount necessarily reaches a plateau when the pore is filled and that the confined fluid reaches its compressibility limit. Although the Freundlich adsorption isotherm provides a quantitative description of simulated or experimental data, it simply consists of an empirical approach which "fits" results for microporous adsorbents.

4. Conclusions

This paper reports an in-depth theoretical study of a realistic model of MCM-41 pores obtained at the atomistic scale using *ab initio* calculations. The structural properties of the realistic model of MCM-41 pores are discussed in terms of X-ray diffraction, small angle neutron scattering, and transmission electron microscopy. We also determine its morphological and textural features using chord length distributions, porous volume, specific geometrical surface, etc. The diffraction pattern of the atomistic model of MCM-41 pores is similar to those obtained for real samples. Strong Bragg peaks corresponding to the {100},

{110}, {200}, and {210} diffraction planes are observed. In addition, peaks obtained at large momentum transfer ($Q > 1$ Å-1) by simulating neutron scattering are in very good agreement with those for bulk amorphous silica. We also found that the Porod exponent $x \sim 3.2$ of the atomistic model (obtained from small angle scattering), which characterizes the surface roughness on length scales from ~ 1 to ~ 10 *nm*, is close to that for real MCM-41 samples. In addition, the simulated TEM image for the atomistic model captures all the features of TEM images for real MCM-41 materials samples (*i.e.*, hexagonal arrangement of cylindrical pores having a uniform pore size, granular textures at the pore surface, etc.). Finally, in order to determine the average silica wall thickness and atomic surface roughness of the MCM-41 model, the density histogram giving the probability to have wall domains of a given density ρ is calculated. While the density in the middle of the pore wall is close to that of amorphous silica $\rho = 2.2$ g/cm^3, the density at the pore surface can be as low as $\rho = 0.5$ g/cm^3 due to important surface roughness. From such calculations, we found that the pore wall thickness d_w $\sim$ 8 - 9 Å is close to the usual experimental values reported in the literature.

In a second part, Grand Canonical Monte Carlo simulations are used to test the degree of realism of the atomistic model of MCM-41 pores by determinig N_2, CO_2, and H_2O adsorption. Both the nitrogen adsorption isotherm at 77 K and water adsorption isotherm at room temperature in the atomistic model of MCM-41 are in fair agreement with available experimental data. At low pressures, a molecular thick film is adsorbed at the pore surface. The thickness of the adsorbed film increases with increasing pressure in the multilayer adsorption regime. Then, at a pressure much lower than the bulk saturating vapor pressure, a sharp increase in the adsorbed amount is observed as capillary condensation within the nanopores occurs. While nitrogen uniformly covers the pore surface prior to capillary condensation, we found that water forms a film adsorbed on specific hydrophilic regions of

the surface while the rest of the surface is depleted in water molecules. This result suggests that the MCM-41 surface is made up of both hydrophilic and hydrophobic patches. For both nitrogen and water, the isosteric heat of adsorption Q_{st} is characteristic of adsorption on heterogeneous surfaces; Qst at low loading is large (due to adsorption in strongly adsorbing sites) and then decreases in a continuous way to a value close to the heat of liquefaction of the gas as further adsorption takes place. Finally, we also found that the BET surface obtained from nitrogen adsorption is an accurate estimate of the specific surface determined from chord length distributions. We also found that nitrogen and water adsorption provide reasonable estimates of the porous volume of porous materials (obtained by converting the amount of adsorbed molecules when the pores are filled into a porous volume using the bulk liquid density). In contrast to nitrogen and water adsorption, the CO_2 adsorption isotherm at room temperature in the atomistic model of MCM-41 materials is reversible and continuous. This result shows that CO_2 confined at room temperature in nanopores of a diameter ~ 3.2 *nm* is above its capillary critical temperature. For each gas, we show that the simulated adsorption/desorption isotherm can be described using availaible theoretical models. In case capillary condensation is observed, the thermodynamical approach proposed a long time ago by Derjaguin also known as the Derjaguin-Broekhoff-De Boer model provides a comprehensive picture of adsorption and capillary condensation in nanopores. On the other hand, we show that the Freundlich equation fits nicely the data for reversible and continuous adsorption isotherms in small nanopores (*i.e.* when capillary condensation is suppressed).

Supporting Information. Intermolecular potentials and BET plot. This material is available free of charge via the Internet at http://pubs.acs.org.

References

(1) Kresge, C. T.; Leonowicz, M. E.; Roth, W. J.; Vartuli, J. C.; Beck, J. S. Ordered mesoporous molecular sieves synthesized by a liquid-crystal template mechanism. *Nature* **1992**, *359*, 710.

(2) Beck, J. S.; Vartulli, J. C.; Roth, W. J.; Leonowicz, M. E.; Kresge, C. T.; Schmitt, K. D.; Chu, C. T. W.; Olson, D. H.; Sheppard, E. W.; McCullen, S. B.; Higgins, J. B.; Schlenker, J. L. A new family of mesoporous molecular sieves prepared with liquid crystal templates. *J. Am. Chem. Soc.* **1992**, *114*, 10834.

(3) Corma, A. From microporous to mesoporous molecular sieve materials and their use in catalysis. *Chem. Rev.* **1997**, *97*, 2373.

(4) Ciesla, U.; Schüth, F. Ordered mesoporous materials. *Microp. Mesop. Mater.* **1999**, *27*, 131.

(5) Soler-Illia, G. J. de A. A.; Sanchez, C.; Lebeau, B.; Patarin, J. Chemical strategiest to design textured materials: from microporous and mesoporous oxides to nano-networks and hierarchical structures. *Chem. Rev.* **2002**, *102,* 4093.

(6) Sonwane, C. G.; Bhatia, S. K.; Calos, N. J. Characterization of surface roughness of MCM-41 using methods of fractal analysis. *Langmuir* **1999**, *15*, 4603.

(7) Berenguer-Murcia, A.; Garcia-Martinez, J.; Cazorla-Amoros, D.; Martinez-Alonso, A.; Tascon, J. M. D.; Linares-Solano, A. About the exclusive mesoporous character of MCM-41.

Studies in Surface Science and Catalysis **144**; F. Rodriguez-Reinoso, B. McEnaney, J. Rouquerol, K. Unger, Eds.; Elsevier Science, **2002**, 83.

(8) Edler, K. J.; Reynolds, P. A.; White, J. W. Small-angle neutron scattering studies on the mesoporous molecular sieve MCM-41. *J. Phys. Chem. B* **1998**, *102*, 3676.

(9) Brodka, A.; Zerda, T. W. Molecular dynamics of SF_6 in porous silica. *J. Chem. Phys.* **1996**, *104*, 6319.

(10) Pellenq, R. J. M.; Levitz, P. E. Capillary condensation in a disordered mesoporous medium: a grand canonical Monte Carlo study. *Mol. Phys.* **2002**, *100*, 2059.

(11) Coasne, B.; Alba-Simionesco, C.; Audonnet, F.; Dosseh, G.; Gubbins, K. E. Adsorption and structure of benzene on silica surfaces and in nanopores. *Langmuir* **2009**, *25*, 10648.

(12) Coasne, B.; Di Renzo, F.; Galarneau, A.; Pellenq, R. J. M. Adsorption of simple fluid on silica surface and nanopore: effect of surface chemistry and pore shape. *Langmuir* **2008**, *24*, 7285.

(13) Gallo, P.; Ricci, M. A.; Rovere, M. Layer analysis of the structure of water confined in vycor glass. *J. Chem. Phys.* **2002**, *116*, 342.

(14) Coasne, B.; Viau, L.; Vioux, A. loading-controlled stiffening in nanoconfined ionic liquids. *J. Phys. Chem. Lett.* **2011**, *2*, 1150.

(15) Siboulet, B.; Coasne, B.; Dufreche, J. F.; Turq, P. Hydrophobic transition in porous amorphous silica. *J. Phys. Chem. B* **2011**, *115*, 7881.

(16) Gelb, L. D.; Gubbins, K. E. Characterization of porous glasses: simulation models, adsorption isotherms, and the Brunauer-Emmett-Teller analysis method. *Langmuir* **1998**, *14*, 2097.

(17) Siperstein, F. R.; Gubbins, K. E. Phase separation and liquid crystal self-assembly in surfactant-inorganic-solvent systems. *Langmuir* **2003**, *19*, 2049.

(18) Coasne, B.; Hung, F. R.; Pellenq, R. J. M.; Siperstein, F. R.; Gubbins, K. E. Adsorption of simple gases in MCM-41 materials: the role of surface roughness. *Langmuir* **2006**, *22*, 194.

(19) Bhattacharya, S.; Coasne, B.; Hung, F. R.; Gubbins, K. E. Modeling micelle-templated mesoporous material SBA-15: atomistic model and gas adsorption studies. *Langmuir* **2009**, *25*, 5802.

(20) Ugliengo, P.; Sodupe, M.; Musso, F.; Bush, I. J.; Orlando, R.; Dovesi, R. Realistic models of hydroxylated amorphous silica surfaces and MCM-41 mesoporous material simulated by large-scale periodic B3LYP calculations. *Adv. Mater.* **2008**, *20*, 1.

(21) Ugliengo, P.; Viterbo, D.; Chiari, G. *Zeitsch. Kristallog.* **1993**, *208*, 383.

(22) Coasne, B.; Galarneau, A.; Di Renzo, F.; Pellenq, R. J. M. Molecular simulation of nitrogen adsorption in nanoporous silica. *Langmuir* **2010**, *26*, 10872.

(23) Potoff, J. J.; Siepmann, J. I. Vapor-liquid equilibria of mixtures containing alkanes, carbon dioxide, and nitrogen. *AIChE J.* **2001**, *47*, 1676.

(24) Berendsen, H. J. C.; Postma, J. P. M.; Gunsteren, W. F.; Hermans, J. *Intermolecular Forces*, Ed. B. Pullman; Reiden: Dordrecht (**1981**).

(25) Harris, J. G.; Jung, K. H. Carbon dioxide's liquid-vapor coexistence curve and critical properties as predicted by a simple molecular model. *J. Phys. Chem.* **1995**, *99*, 12021.

(26) Rodriguez-Carvajal, J. Recent developments of the program FULLPROF. *Comm. Powder Diffr. Newsletter*, 2001, **26**, 12.

(27) Ramsay, J. D. F. Surface and pore structure characterisation by neutron scattering techniques. *Adv. Colloid Interface Sci.* **1998**, *76-77*, 13.

(28) Wright, A. C.; Sinclair, R. N. Neutron scattering from vitreous silica. *J. Non Cryst. Sol.* **1985**, *76*, 351.

(29) Levitz, P.; Ehret, G.; Sinha, S. K.; Drake, J. M. Porous vycor glass: the microstructure as probed by electron microscopy, direct energy transfer, small-angle scattering, and molecular adsorption. *J. Chem. Phys.* **1991**, *95*, 6151.

(30) Mitropoulos, A. C.; Haynes, J. M.; Richardson, R. M.; Kanellopoulos, N. K. Characterization of porous glass by adsorption of dibromomethane in conjunction with small-angle x-ray scattering. *Phys. Rev. B* **1995**, *52*, 10035.

(31) Drake, J. M.; Levitz, P.; Klafter, J. Molecular adsorption on porous silica gels from binary solutions. *Isr. J. Chem.* **1991**, *31*, 135.

(32) Pikunic, J.; Clinard, C.; Cohaut, N.; Gubbins, K. E.; Guet, J. M.; Pellenq, R. J.-M.; Rannou, I.; Rouzaud, J. N. Structural modeling of porous carbons: constrained Reverse Monte Carlo method. *Langmuir* **2003,** *19, 8565.*

(33) Kruk, M.; Jaroniec, M.; Sakamoto, Y.; Terasaki, O.; Ryoo, R.; Ko, C. H. Determination of pore size and pore wall structure of MCM-41 by using nitrogen adsorption, transmission electron microscopy, and X-ray diffraction. *J. Phys. Chem. B* **2000,** *104, 292.*

(34) Levitz, P. Off-lattice reconstruction of porous media: critical evaluation, geometrical confinement and molecular transport. *Adv. Coll. Interface Sci.* **1998**, *76-77*, 71.

(35) Connolly, L. M. Solvent-accessible surfaces of proteins and nucleic acids. *Science* 1983, *221*, 709.

(36) Rouquerol, F.; Rouquerol, J.; Sing, K. S. W. Adsorption by Powders and Porous Solids; Academic Press: London, **1999**.

(37) Galarneau, A.; Cambon, H.; Di Renzo, F.; Fajula, F. True microporosity and surface area of mesoporous SBA-15 silicas as a function of synthesis temperature. *Langmuir* **2001**, *17*, 8328.

(38) Rotenberg, B.; Patel, A. J.; Chandler, D. Molecular explanation for why talk surfaces can be both hydrophilic and hydrophobic surfaces. *J. Am. Chem. Soc.* **2011**, *133*, 20521.

(39) Inagaki, S.; Fukushima, Y.; Kuroda, K.; Kuroda, K. Adsorption isotherm of water vapor and its large hysteresis on highly ordered mesoporous silica. *J. Coll. Interface Sci.* **1996**, *180***,** 623.

(40) Chen, C. Y.; Li, H. X.; Davis, M. E. Studies on mesoporous materials I: synthesis and characterization of MCM-41. *Microporous Materials* **1993**, *2*, 17.

(41) Coasne, B.; Gubbins, K. E.; Pellenq, R. J. M. Temperature effect on adsorption/ desorption isotherms for a simple fluid confined within various nanopores. *Adsorption* **2005**, *11*, 289.

(42) Ho, N. L.; Perez Pellitero, J.; Porcheron, F.; Pellenq, R. J. M. Enhanced CO_2 solubility in hybrid MCM-41: molecular simulations and experiments. *Langmuir* **2011**, *27*, 8187.

(43) Derjaguin, B. V.; Churaev, N. V. Polymolecular adsorption and capillary condensation in narrow slit pores. *J. Colloid Interface Sci.* **1976**, *54*, 157.

(44) de Gennes, P. G. Wetting : statics and dynamics. *Rev. Modern Phys.* **1985**, *57*, 827.

(45) Charlaix, E.; Ciccotti, M. Capillary condensation in confined media. *Handbook of Nanophysics: Principles and Methods*, Ed. Klaus Sattler. CRC Press, **2010**.

(46) Saugey, A. PhD Thesis "Etudes des systèmes matériaux nanoporeux – liquides non mouillants". Ecole Centrale de Lyon, **2004**.

(47) Pellenq, R. J. M.; Coasne, B.; Denoyel, R. O.; Coussy, O . Simple phenomenological model for phase transitions in confined geometry. 2. Capillary condensation/evaporation in cylindrical mesopores. *Langmuir* **2009**, 25, 1393.
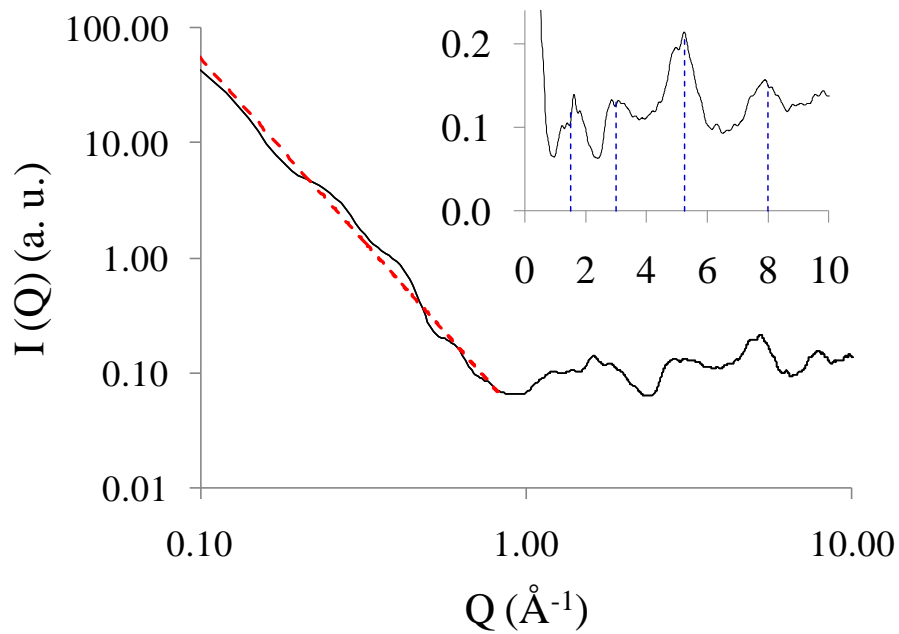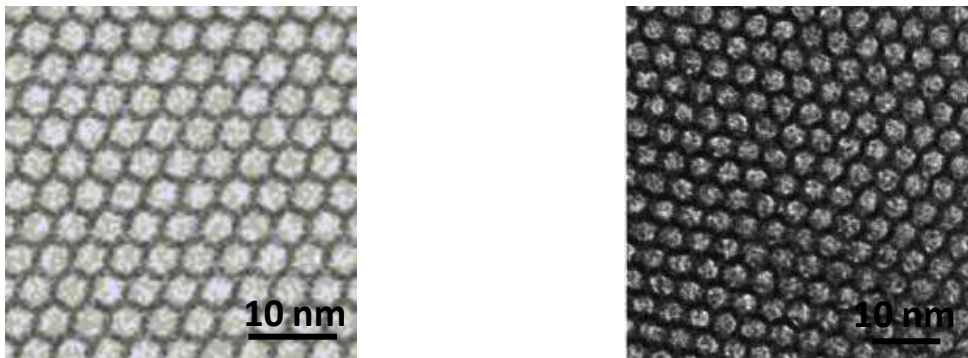
Figures.
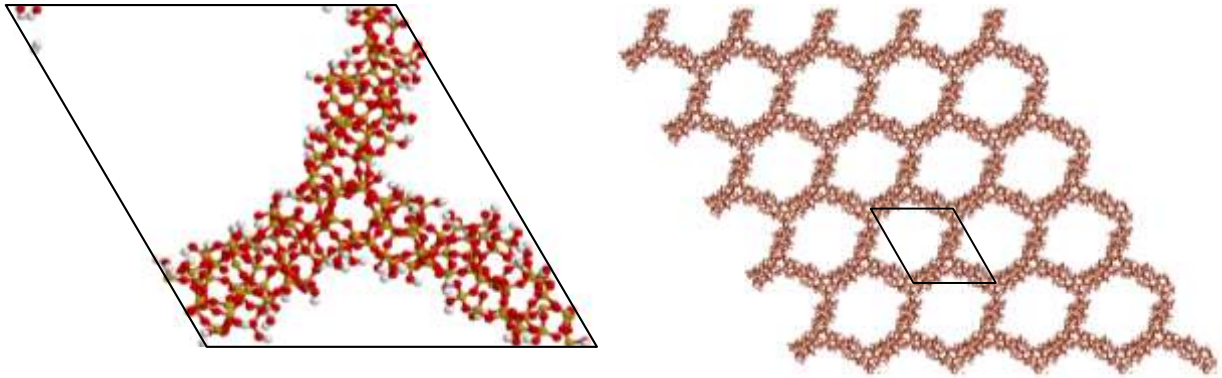
Figure 1. (left) Unit cell of the atomistic model of micelle-templated mesoporous silica MCM-41. The unit cell consists of a hexagonal structure with $a = b = 4.0603039$ *nm* and $c = 1.2200913$ *nm*. The unit cell of a volume $V = 52.3$ *nm*^{3} contains 102 H atoms (white spheres), 335 O atoms (red spheres), and 142 Si atoms (orange spheres). (right) Simulation box obtained by duplicating 5 times the unit cell corresponding to the black hexagon in the *x* and *y* directions.
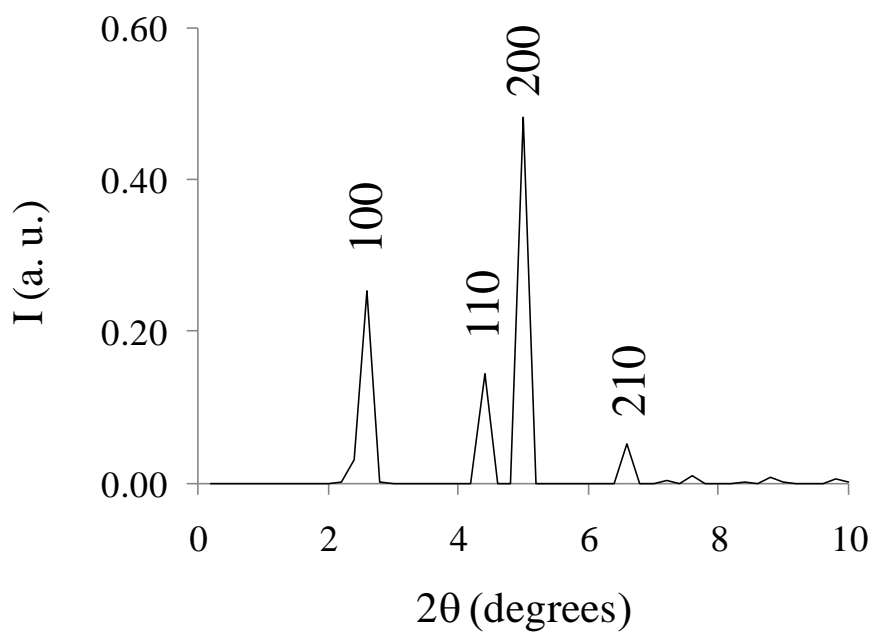
Figure 2. X-ray diffraction pattern of the atomistic structural model of MCM-41 materials**.** The latter diffraction pattern was obtained for a wavelength $\lambda = 1.54$ Å (corresponding to Copper CuKα).

Figure 3. Small angle neutron scattering spectrum of the atomistic model of MCM-41 materials (black line)**.** The dashed red line corresponds to an algebraic decay over the range 0.1-1 Å^{-1} with the Porod exponent $x = 3.2$ (*see text*). The inset displays the same small angle neutron spectrum in a linear scale. The Bragg peaks for the atomistic model of MCM-41 materials are in agreement with the experimental peaks indicated by the blue dashed lines: [28] 1.5 Å^{-1}, 3.0 Å^{-1}, 5.25 Å^{-1} and 8.0 Å^{-1}.

Figure 4. (left) Simulated TEM image of the atomistic structural model of MCM-41 materials. (right) Experimental electron microscopy of MCM-41 having a pore diameter $D = 2.0$ nm (adapted from Kruk et al.[33]). Note that the structural model has larger pores than in the experiments.
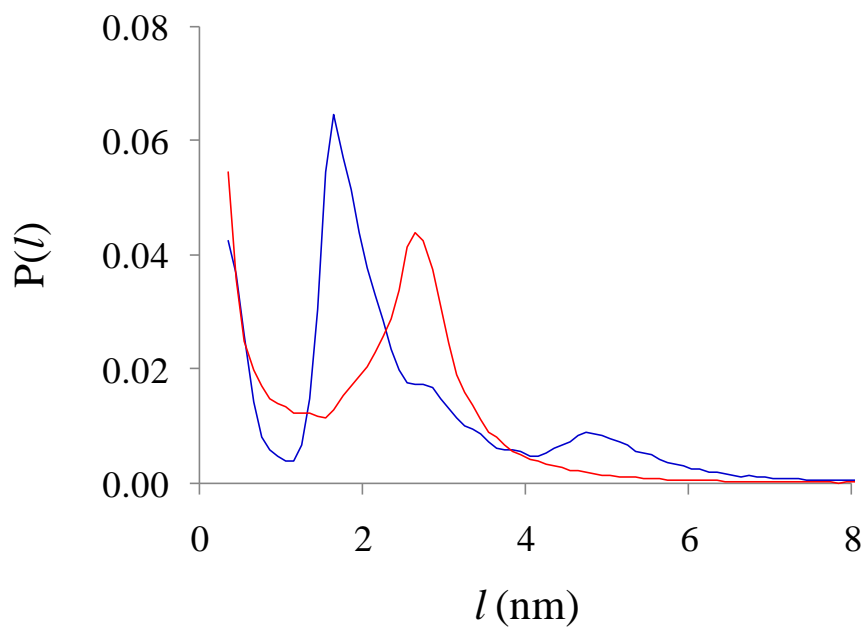
Figure 5. In-pore (red line) and in-wall (blue line) chord length distributions for the atomistic structural model of MCM-41 materials. The *y* axis is in arbitrary units.
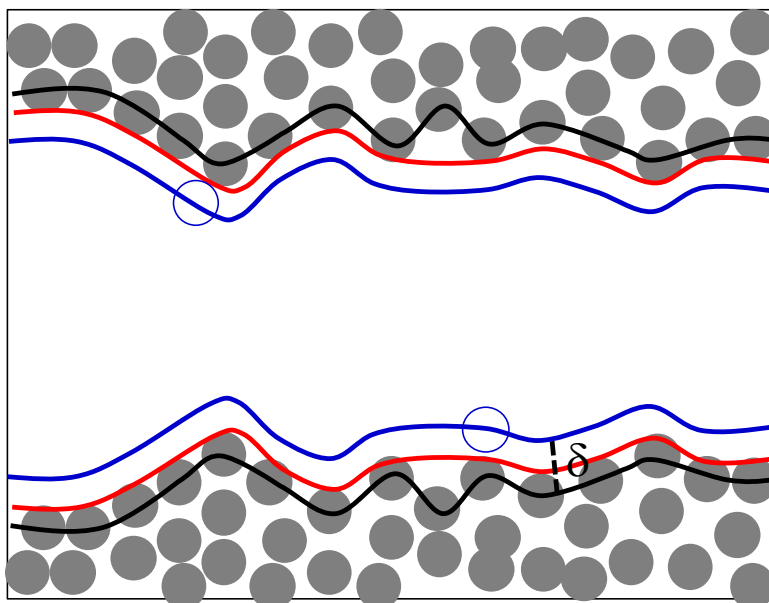
Figure 6. Definition of the porous volume V_{sp} and geometrical surface S_{sp} accessible to an adsorbate molecule whose distance with matrix atoms cannot be smaller than δ. The grey circles are the matrix atoms of the porous materials. The blue circles are adsorbate molecules. The black line corresponds to the line passing through the center of mass of the surface matrix atoms. The blue line corresponds to the specific surface S_{sp} of the porous material which is obtained from the trajectory of the center of mass of the adsorbate molecule as it rolls over the porous surface. In contrast, the red line, which corresponds to Connolly's surface, is the contact surface covered by an adsorbate molecule as it rolls over the surface. Using the same procedure, one obtains the volume enclosed between the red lines which corresponds to the porous volume of the sample accessible to a molecule whose distance with the matrix atoms cannot be smaller than δ.
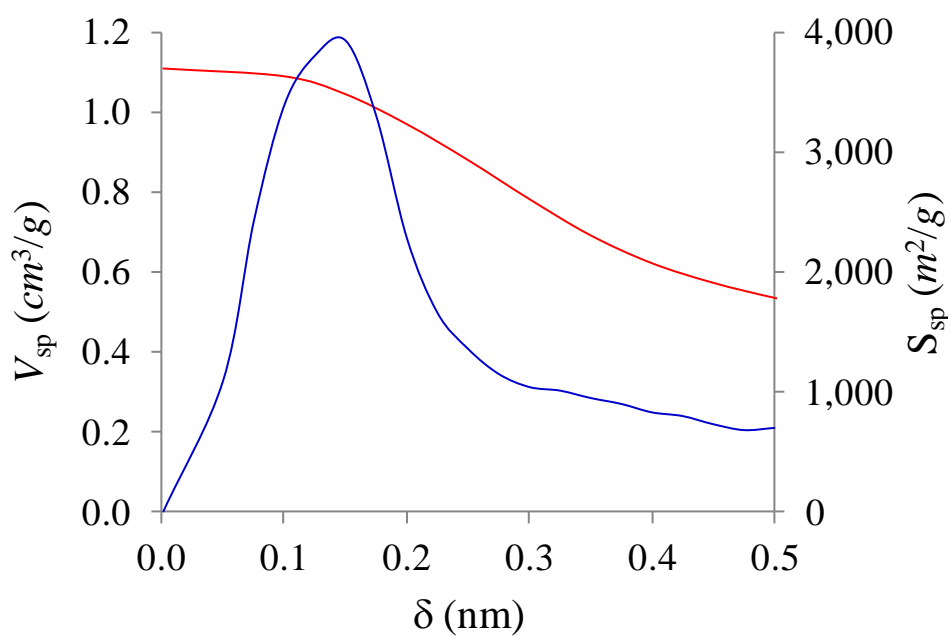
Figure 7. Porous volume V_{sp} (red curve, left axis) and geometrical surface S_{sp} (blue line, right axis) of the atomistic structural model of MCM-41 materials as a function of the size δ of the probe molecule (*see text*).
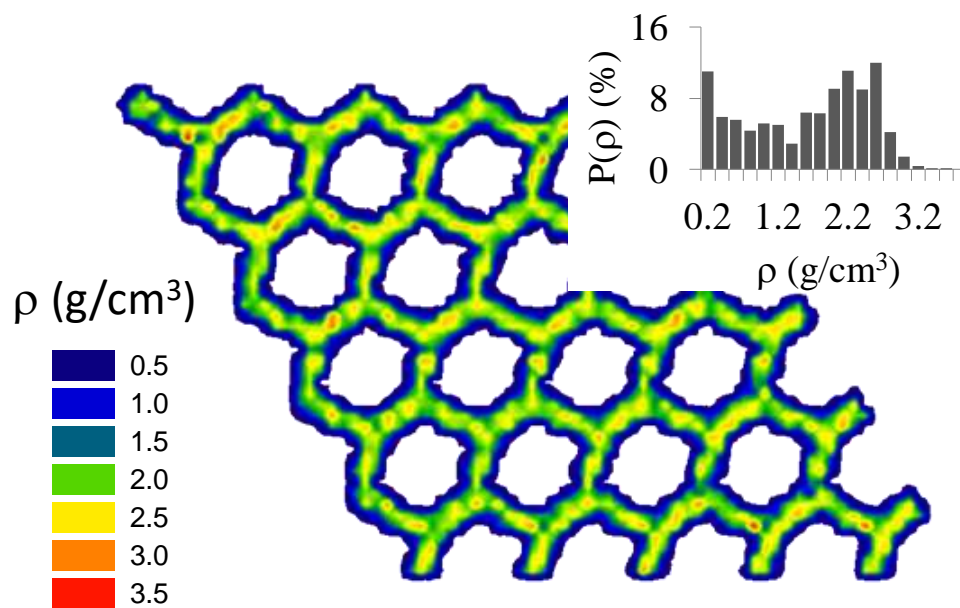
Figure 8. Density contour plot of the silica wall of the atomistic structural model of MCM-41 materials. The color scale varies linearly with the density in *g/cm³*. The inset shows the density histogram $P(\rho)$ defined as the percentage of wall domains of a density ρ (a domain is a small volume element ~3 *nm³*).
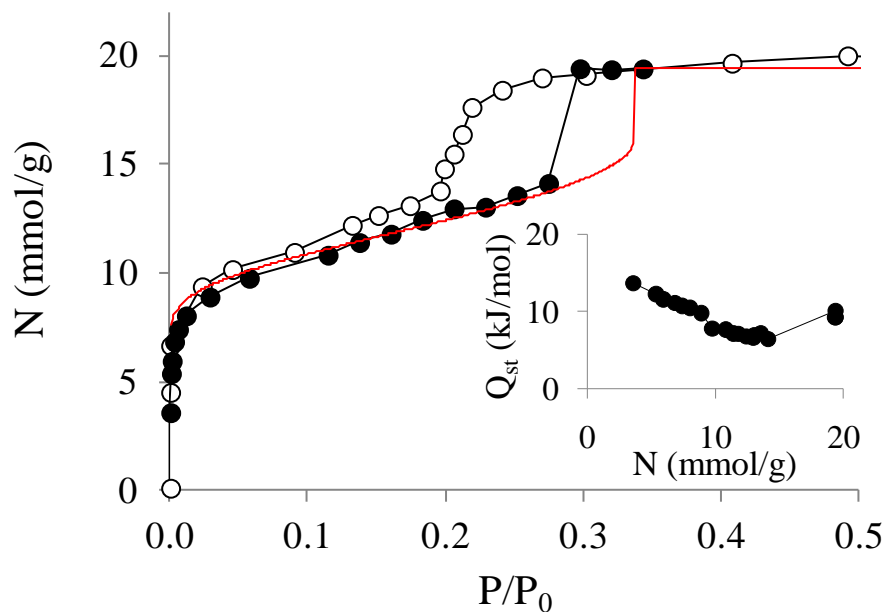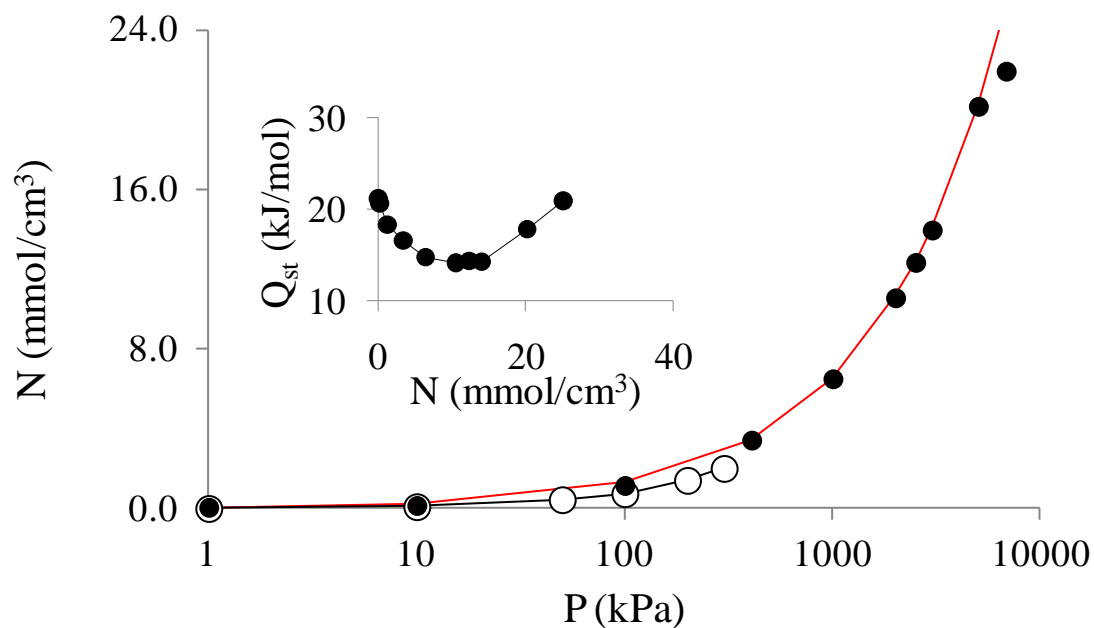
Figure 9. N_2 adsorption isotherm at 77 K in the atomistic model of MCM-41 materials (black circles). The open circles are experimental data obtained for MCM-41.[33] The red line corresponds to the theoretical model based on Derjaguin's approach (*see text*). The insert shows the isoteric heat of nitrogen adsorption at 77 K in the atomistic model of MCM-41 materials.
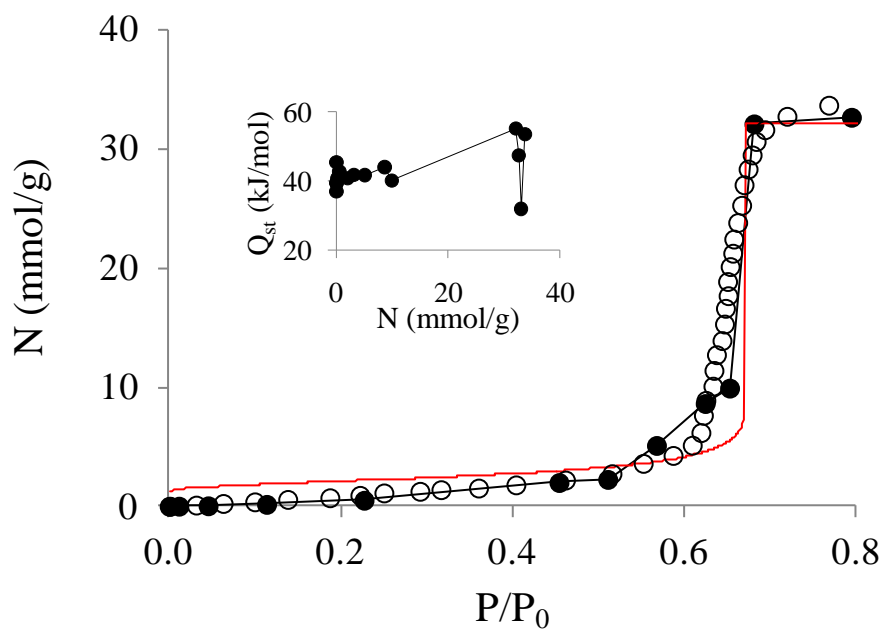
Figure 10. Water adsorption isotherm at 300 K in the atomistic structural model of MCM-41 materials (black circles). The open circles are experimental data for MCM-41.[39] The red line corresponds to the theoretical model based on Derjaguin's approach (*see text*). The insert shows the isosteric heat of water adsorption at 300 K in the atomistic model of MCM-41 materials.
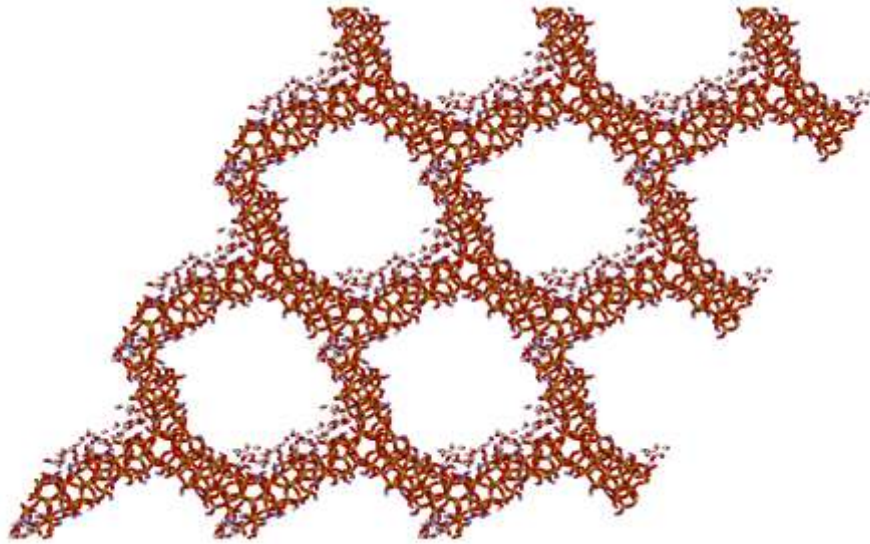
Figure 11. Typical molecular configuration of water adsorbed at room temperature and a pressure $P = 2000$ Pa (0.45 P_0) in the atomistic model of MCM-41 pores. The silica matrix corresponds to the segments between the Si, O, and H atoms shown as orange, red, and blue sticks. The red – white segments correspond to the OH bonds of the adsorbed water molecules. One sees that water forms a film adsorbed on specific hydrophilic regions of the surface while the rest of the surface is depleted in water molecules Note that the simulation box (unit cell) has been duplicated 3 times in the *x* and *y* directions for visualization purpose.

Figure 12. CO_2 adsorption isotherm at 303.15 K in the atomistic model of MCM-41 materials (black circles). The open circles are experimental data by Ho et al. for CO_2 adsorption at 303.15 K in MCM-41.[42] The red line corresponds to the fit of the simulated data using the Freundlich equation for adsorption. The insert shows the isosteric heat of CO_2 adsorption at 303.15 K in the atomistic model of micelle-templated mesoporous silica MCM-41.

TOC Figure

Benoit Coasne* and Piero Ugliengo

Atomistic model of micelle-templated mesoporous silicas: Structural, morphological and N$_2$, CO$_2$, H$_2$O adsorption properties.

Structural, morphological and adsorption properties of porous silica. The structure and morphology of a realistic model of MCM-41 mesoporous silicas are determined by simulating neutron scattering, X-ray diffraction, electronic microscopy and by calculating chord length distributions, surface area, porous volume, etc. N$_2$, CO$_2$ and H$_2$O adsorption are simulated and compared with experimental data and theoretical models of adsorption in nanopores.

N$_2$, CO$_2$, H$_2$O Adsorption

Neutron scattering